Local nearly non-strained perovskite lattice approaching a broad environmental stability window of efficient solar cells

Jie Xu [a], Hua Dong [a,c,**], Jun Xi [e], Yingguo Yang [d], Yue Yu [f], Lin Ma [f], Jinbo Chen [a], Bo Jiao [a], Xun Hou [a], Jingrui Li [b,***], Zhaoxin Wu [a,c,*]

[a] Key Laboratory for Physical Electronics and Devices of the Ministry of Education & Shaanxi Key Lab of Information Photonic Technique, School of Electronic and Information Engineering, Xi'an Jiaotong University, No.28, Xianning West Road, Xi'an, 710049, China
[b] Electronic Materials Research Laboratory, Key Laboratory of the Ministry of Education & International Center for Dielectric Research, School of Electronic Science and Engineering, Xi'an Jiaotong University, Xi'an, 710049, China
[c] Collaborative Innovation Center of Extreme Optics, ShanxiUniversity, Taiyuan, 030006, China
[d] Shanghai Synchrotron Radiation Facility, Shanghai Institute of Applied Physics, Chinese Academy of Sciences, Shanghai, 201204, China
[e] Zernike Institute for Advanced Materials, University of Groningen, Nijenborgh 4, 9747, AG, Groningen, the Netherlands
[f] School of Physics and Optoelectronic Engineering, Xidian University, Xi'an, 710071, China

ARTICLE INFO

ABSTRACT

Twist and fracture of surface lattice tend to occur under harsh condition due to the soft lattice natures of hybrid perovskite materials. Accordingly, surface defects and lattice distortion are produced, which allow the performance loss and notorious degradation in perovskite solar cells (PSCs). In our work, judiciously selected conjugated ligand was employed as the film intermediary, from which rigid and delocalization 4-phenylpyridine (4-pPy) exhibited the most significant improvement on both optoelectrical performance and stability of PSCs. By regulating the film crystallization kinetics, high-quality perovskite films can be obtained with preferable crystal orientation. Moreover, benefiting from the defects passivation and unidirectional bonding effect, coordinated 4-pPy "scaffold" on the lattice surface could mitigate vacancy formation and lattice twist/fracture under severe conditions. The resulted p-i-n planar device shows a considerable PCE of 21.12% (certified 20.2%) with negligible hysteresis, as well as an excellent storage (90% of original PCE after 1000 h at 60% RH), operating (90% of original PCE after 600 h at maximum power point) and thermal stress (89% of original PCE after 500 h at 85 °C) stability. It is hoped that our findings could open a new way to accelerate continued progress on PSCs regimes for efficieny maximization and stability prolongation.

1. Introduction

Organic-inorganic metal halide perovskite materials are emerging as a superstar in the field of photoelectric devices, such as solar cells, light-emitting diodes, sensors and laser, owing to the advantages of ideal direct energy band, high absorption coefficient, tunable bandgap and high carrier mobility [1–10]. Benefiting from the excellent photoelectric characteristics of perovskite materials, a record efficiency of 25.2% has been reached [11]. Nevertheless, how to further improve the photo-thermal stability and approach the Schockley-Queisser (SQ) efficiency

limit of the PSCs is still challenging for commercial applications [12,13].

Afflicted by the low formation energy and rapid crystallization rate of hybrid perovskite materials, as-prepared polycrystalline films always accompanied involvement with poor morphology and excessive grain boundaries (GBs), that is, high defect density and low crystallization quality [14,15]. Notably, traps-induced nonradiative recombination on the surface/GBs of the perovskite strongly restricted the enhancement of device performance. Moreover, considering the uncoordinated Pb naked on the surface of lattice unit, the chemical bonding between metal-iodide is vulnerably deformation rupture, leading to the ion

migration and components volatilization. When undergoing the harsh conditions (thermal stress, illumination or bias-voltage applied), the deterioration of the structure distortion would further deteriorate, causing the rapid performance degradation and materials decomposition.

Recently, different approaches have been exploited to improve the device performance and stability, of which the popular Lewis acid-base additive has been developed a common means to form the dense and smooth high-quality perovskite films by adjusting crystallization process. Till now, pyridine and aniline with N-donor bases [16,17], thiourea and thioacetamide with S-donor bases [18], DMSO, N-methyl-2--pyrrolidone (NMP) and urea with O-donor bases [19,20], have been reported to passivate undercoordinated Pb^{2+} defects through hydrogen bonding. Meanwhile, in terms of chemical additive approachs, halogenoid, such as (SCN)⁻, incorporation introduced into perovskite can regulate the crystal nucleation-growth process, enlarge grain size and nearly eliminate grain boundaries [21–23]. In addition, in order to improve the device stability of the device, the interface engineering of

ligand molecules and the construction of low-dimensional perovskite active layer can are adopted, which could effectively improve resist ambient factors, including water, oxygen, light and heat stability. Particularly, large-sized cation such as 5-ammoniumvaleric acid (AVAI) [24], phenethylammonium (PEA) [25], polyethylenimine (PEI) [26], n-butylammine (BA) [27], cyclopropylamine (CA) [28] and octadecyl-amine (OA) [29] are available to be incorporated into perovskite or interface, further enhancing the stability. Although ligand engineering is involved to improve PSCs, fundamental understanding of the film crystallinity and chemical interaction dependent on the geometrical configuration and electrical structure of ligand molecules is highly imperative to study.

In our work, we employ a series of pyridine derivatives (Py-derivatives) as the precursor additives, achieving the dual regulation of film crystallization kinetics and lattice stabilization. As the typical lewis base, chelating Py-derivatives could effectively adjust the competition of nucleation and growth, thus contributing to the high-quality polycrystalline films with large-scale grains and ordered crystal orientation.
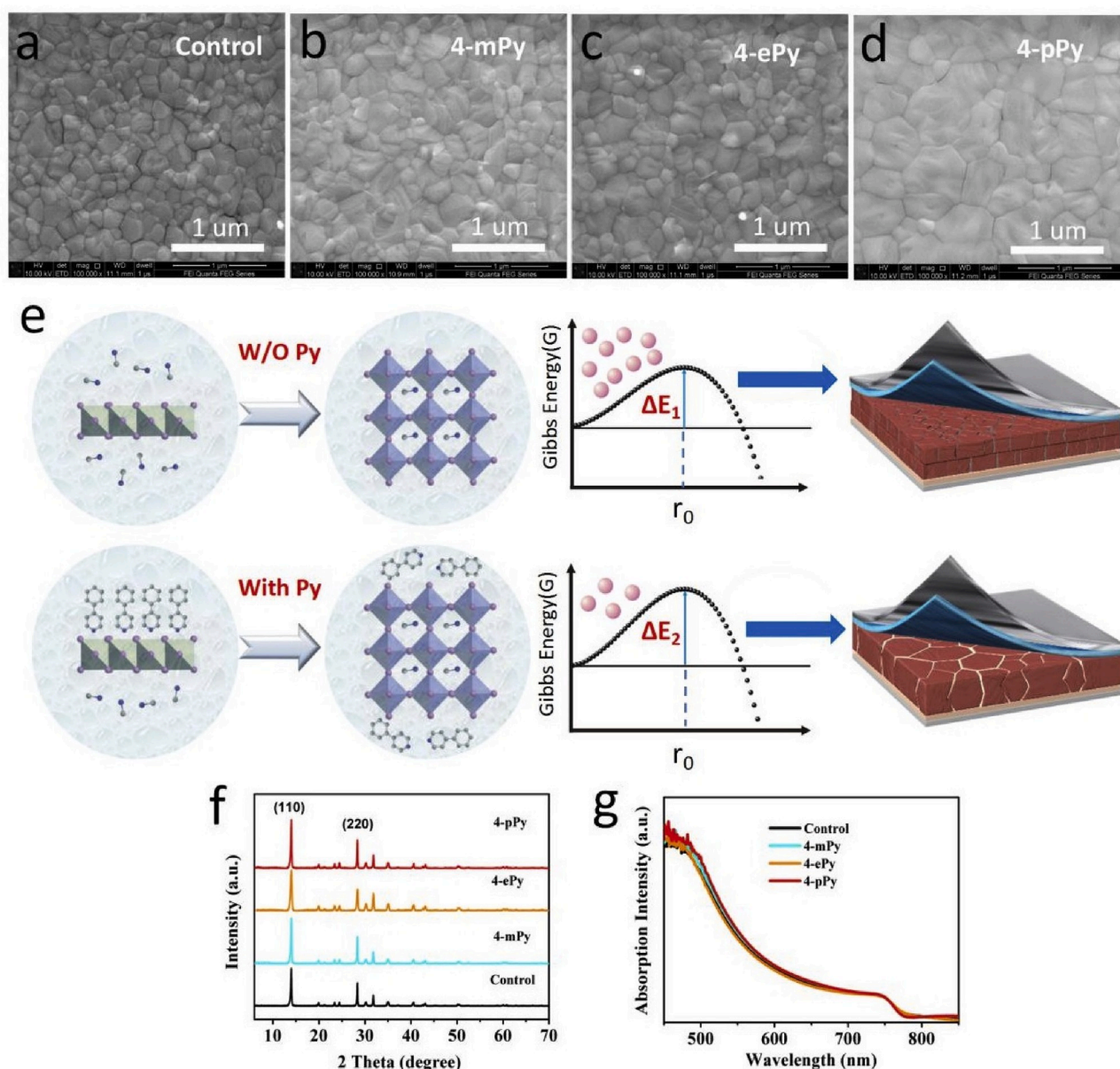

Fig. 1. (a-d) SEM images of controlled and Py-derivates modified perovskite films. (e) The reaction coordinate diagram of the perovskite formation via the conventional and pyridine-regulated pathway. (f) XRD patterns and (g) absorption spectrum of controlled and Py-derivates modified perovskite films.

Furthermore, reserved ligands anchoring on the surface/GBs of the as-prepared film could work as the "encapsulate frame", benefiting not only the electrical characteristic but structure robustness. Regardless of the harsh conditions of high-temperature or illumination, performance degeneration and material decomposition were greatly alleviated. Owing to the conjugated and delocalized characteristics of the molecule, 4-phenylpyridine exhibited the synthetical effects on crystallization quality, defect inhibition and lattice robustness of the perovskite film. Finally, we achieved an enhanced 21.12% (20.2% certified) device efficiency, as well as excellent humidity, thermal and operating stability. Such champion efficiency retained ~90% of its original value after 600 h of continuous illumination under maximum power point (MPP) operating conditions, or under thermal stress of 85 °C.

2. Results and discussion

2.1. Crystallization kinetics

In our study, the conventional one-step anti-solvent solution method was carried out to prepared the $MAPbI_3$ perovskite absorber. In view of the chelation effect between pyridine group and Pb atom, a series of Py-derivatives (4-methylpyridine (4-mPy), 4-ethylpyridine (4-ePy) and 4-phenylpyridine (4-pPy)) (molecule structures shown in Fig. S1)were introduced to the perovskite precursor, which was supposed assuming as the intermediary for the film crystallization process. Fig. 1a–d present the morphological variation evolution of perovskite films with assisted by different types of Py-derivatives additives. It can be observed that all three ligands contributed to the dense and large-scales morphology. In Fig. S2, we also give the distribution diagram of grain size without and with additives. Especially, in the 4-pPy modified film, uniform and micrometer-scale grains were obtained. It is well known that the dominated defects are located on the surface and GBs of the perovskite bulk. Hence the enlarged crystal grains (less GBs) are allowed to reduce traps density. However, in Fig. S3, with the increase of concentration, the surface morphologies of perovskite film become rougher, increasing the number of surface defects.

Since these additives have the same concentrations, the essence of morphology difference is worth study. In general, the kinetics of the crystal growth process was embodied in the synthetical actions of the crystal nucleation and growth. Naturally, the faster nucleation rate of hybrid perovskite material was easy to cause relatively small crystal grains. In the commencement of film formation process (one-step method), three reactions run as follows:

$$PbI_2 + MAI \rightarrow MAPbI_3 \qquad (1)$$

$$PbI_2 + x\text{-}Py \rightarrow x\text{-}Py \cdot PbI_2 \qquad (2)$$

$$x\text{-}Py \cdot PbI_2 + MAI \rightarrow MAPbI_3 + x\text{-}Py \qquad (3)$$

The first and third reaction are positive processes for forming perovskite nucleus, while the second reaction plays a negative role. As for these three Py-derivatives, different geometrical configurations may affect the coordination between ligands and metal halides. We calculated the reaction energies between the PbI_2 at the surface of the perovskite ($MAPbI_3$) and different ligands using density functional theory (DFT). The results are −2.10, −2.07 and −2.37 eV for 4-mPy, 4-ePy and 4-pPy, respectively, compared with −1.05 eV for MAI. It can be observed that 4-pPy exhibits the strongest chemical interaction with PbI_2 among three ligands on account of its conjugated and rigid structure. Therefore, the addition of the Py-derivatives significantly retarded the perovskite crystallization course, which contributes to the uniform and large-scale polycrystalline film (Gibbs free energy diagrams of perovskite nucleation and growth shown in Fig. 1e). Notably, 4-pPy molecular provided the highest nucleation energy barrier, resulting in the largest grain distribution.

Afterward, the crystallinities of the various perovskite films were

investigated by X-ray diffraction analysis, whose results are shown in Fig. 1f. As for all Py-modified films, the intensity of (110) diffraction peak was enhanced by different degrees. The full width at half maximum (FWHM) of the main peak was estimated as 0.242°, 0.181°, 0.188° and 0.142° for Control, 4-mPy, 4-ePy and 4-pPy, respectively (shown in Fig. S4). The FWHM variation of the XRD reveals that the introduction of the Py-derivatives has a positive effect on improving the quality of the perovskite film. Importantly, the crystallinity trend is consistent with the morphological variation. As for the optical feature, the absorption spectrum of different films was shown in Fig. 1g. Here the controlled and modified films exhibit a similar profile with an absorption band-edge with 780 nm, and overall absorbance was almost invariant. Thus, the optical contribution of modified perovskite layer was negligible via crystallization regulation process.

The crystallographic orientation of perovskite polycrystalline films, as the further embodiment of crystal quality, also has important implications in the performance of PSCs. To precisely study the crystal orientation of different film impacted by Py-derivatives, grazing-incidence wide-angle X-ray scattering (GIWAXS) measurements were performed and the corresponding results of which are shown in Fig. 2a-d. The azimuthally integrated scattering intensities of different GIWXAS patterns are plotted in Fig. 2e along the ring around $q_{xy} = 10 \ nm^{-1}$, assigning to the (110) planes of corresponding perovskites structures. Compared with the plots with gentle fluctuation in controlled film, related sharp signal was observed in the Py-derivatives modified films, indicating the preferential preferred crystallographic orientations [30]. With regard to the electrical in PSCs, ordered crystallographic orientation is in favor of charge transport efficiency in the perovskite bulk, contributing to better performances of PSCs. The cross-sectional SEM image is shown in Fig. 2g. Compared with the irregularly grew crystal grains in controlled film, 4-pPy modified crystal grain delivered suberect and run-through morphology. The cross-section topographic change hence corresponds well with crystal orientation in Fig. 2f.

Considering the comprehensive research of film morphology and crystal quality, Py-derivatives could play important roles in governing the morphology evolution and inducing the crystallization orientation, and reinforcing the potential of defects suppression and charge-transporting acceleration. In this case, a respectable device performance enhancement can be anticipated.

2.2. Device performance

To study the impact of pyridine derivatives on photovoltaic performance, we fabricated inverted planar PSCs with a configuration of Glass/ITO/PTAA/$MAPbI_3$/C_{60}/BCP/Ag, whose schematic diagram of device structure and energy level are shown in Fig. 3a and b. Here 30 samples were prepared for each structure to research reproducibility of devices, and the corresponding parameters of which are summarized in Fig. S5. The representative current density-voltage (J-V) curves of PSCs with made from controlled and modified perovskite films by reverse scan are presented in Fig. 3c. The controlled device showed a PCE of 19.15% with a short-circuit current density of 22.69 mA cm^{-2}, an open-circuit voltage of 1.05 V, and a fill factor of 80.4%. Compared to the controlled device, representative devices incorporated with 4-mPy, 4-ePy and 4-pPy exhibited the improved PCE as 20.40% (22.88 mA cm^{-2},1.09 V, 81.8%), 19.83% (22.70 mA cm^{-2}, 1.08 V, 80.9%) and 21.12% (23.33 mA cm^{-2}, 1.10 V, 82.3%), respectively, whose detailed parameters are presented in Table S1. Impressively, the device modified by 4-pPy instead of others showed the best performance.

Fig. 3d shows the champion device with 4-pPy film and controlled device under the reverse and forward scan, respectively. Besides, whose detailed parameters are presented in Table S2. As for the best performance of 4-pPy, device results of an efficiency of 21.12% (21.07%) under reverse (forwarding) scan with a short-circuit current density of 23.33 (23.32) mA cm^{-2}, an open-circuit voltage of 1.10 (1.11) V, and a fill factor of 82.3 (81.4)% was obtained which is with negligible
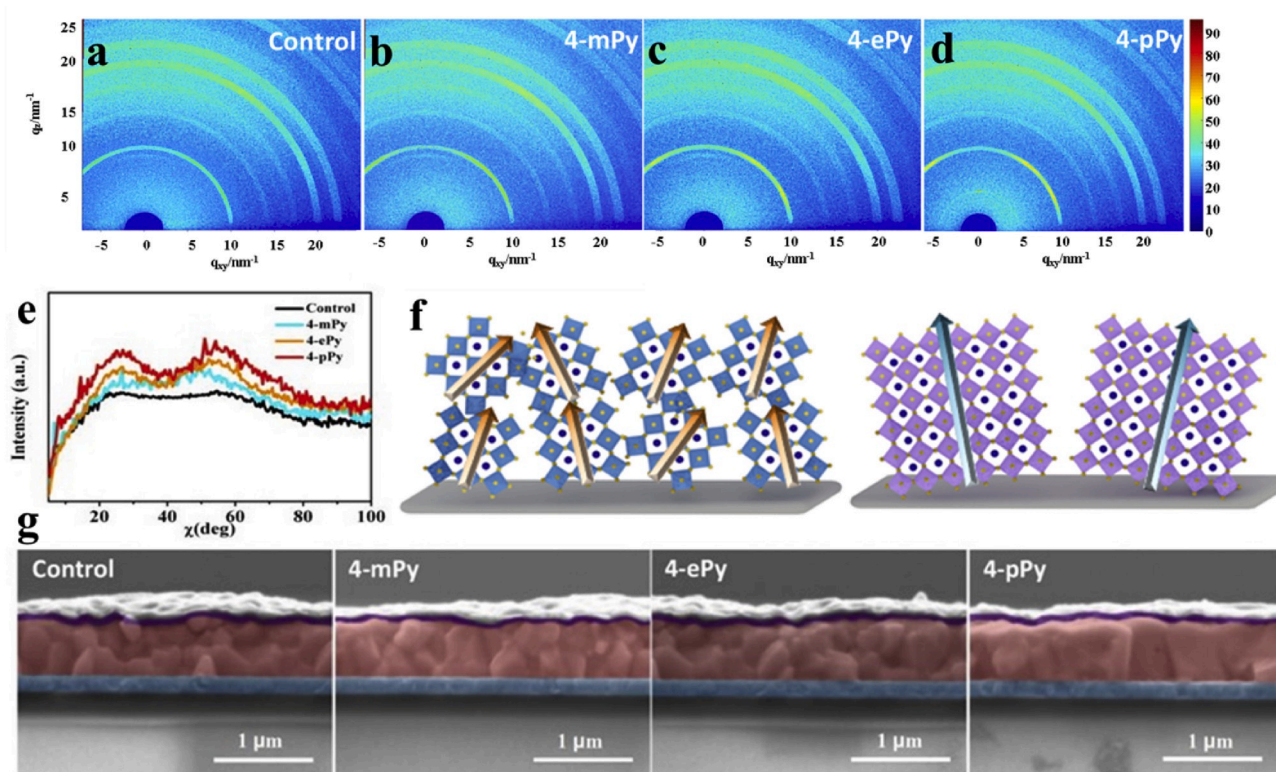
Fig. 2. (a-d) GIWAXS patterns of controlled and Py-derivates modified perovskite films. (e) Radially integrated intensity plots along the ring at $q = 10$ nm^{-1}, assigned to the (110) plane of MAPbI$_3$. (f) Grain crystals stacking modes for the controlled and Py-derivates modified perovskite films. (g) The cross-sectional images of PSC devices without (Controlled) and with pyridine derivatives (4-mPy, 4-ePy, 4-pPy), respectively.

hysteresis. In comparison, control devices still exhibit obvious hysteresis. To verify the J-V scanning, the incident photo-to-electron conversion efficiency (IPCE) spectra of the cell with 4-pPy-treated (control) was evaluated, as shown in Fig. 3e. The integrated short-circuit current density was calculated to be 22.39 (21.66) mA cm^{-2}, matching well with the obtained short-circuit current density. Meanwhile, the steady-state photocurrent of 4-pPy-treated (control) device at MPP is in good agreement with J-V scanning in Fig. 3f, also suggesting a stable short-circuit current of 22.00 (21.20) mA cm^{-2}. In addition, the steady-state PCE of 4-pPy-treated (control) device at MPP is in good agreement with J-V scanning in Fig. S6, also suggesting a stable PCE of 20.94% (19.03%).

To confirm our in-laboratory device efficiency measurements, we sent our non-encapsulated devices to the National Institute of Metrology, China, for external certification and obtained a PCE of 20.2% (Voc = 1.099 V, Jsc = 22.92 mA cm^{-2}, and FF = 80.4%) in Fig. S7.

2.3. Defects states and charge dynamic

In spite of improved morphology and crystallinity assisted by all three Py-derivatives, the device performance with alkyl-pyridine (4-ePy and 4-mPy) does not significantly change. Here the inconsistency is worth pondering. Considering the coordinate ability between the nitrogen atom of Py-derivatives and lead atom of perovskites. Py-derivatives are supposed to play multiple roles besides the film formation intermediary. To prove whether Py-derivative is incorporated within the ultimate product, the Fourier-transform infrared (FTIR) spectra of controlled and modified perovskite films were carried out and shown in Fig. 4a. The characteristic C=N stretching vibration of Py-derivative nearly 1,590 cm^{-1} was not observed in controlled film [31]. However, this fingerprint peak emerged and shifted to a higher wavenumber in all three modified films, as an indicative of the bonding behavior between perovskite framework and the pyridine ring. X-ray photoelectron spectroscopy (XPS) is also conducted to verify the ligands-to-perovskite interaction in Fig. 4b. Comparing with the controlled films, the phenomenon that signals of Pb 4f shifted from 138.3 eV to 143.1 eV was observed in Py-derivatives modified films, implying the variation of chemical bonding [32]. Especially, two small peaks located at 136.5 and 141.4 eV were observed the in controlled sample, suggesting the existence of metallic Pb [33]. However, the peak intensity was significantly decreased in the modified films, such diminution strongly implies the elimination of the iodide vacancies in the perovskite lattice. Based on the comprehensive investigation by FTIR (Fig. S8), XPS(Fig. S9) and XRD, one can easily conclude that a portion of Py-derivatives participated in the composition of the prepared polycrystalline films. By interacting with the uncoordinated Pb, the existence of Py-derivatives act as"scaffold" anchoring on the surface of the perovskite lattices.

Since Py-derivatives have been verified to exist in the ultimate perovskites, it is highly motivated to figure out the potential effect of the intrinsic characteristics of molecular level, which could greatly affect trap-induced recombination and charge-transporting behaviors. To gain insight into the chemical coordination, geometrical configuration and electrostatic states features of different Py-derivatives influencing the device performance, a series of theoretical and experimental strategies were carried out. The vacancy defects in the perovskites could act as the non-radiative recombination centers which injured the device performance [34]. We calculated the formation energies of iodide vacancies in different perovskite films using density functional theory (DFT, see Methods and Supplementary Data 1). The formation energy involved with iodide vacancies is remarkably low (~0.81 eV) in controlled film. In the modified modeling atomic structures, the surfaces of the large supercells are passivated by various Py ligands. The corresponding iodide vacancy formation energy is increased more than several folds, estimated as 1.44eV (4-mPy), 1.41eV (4-ePy) and 1.49eV (4-pPy), respectively. The DFT calculation results (Fig. 4c) correspond to the
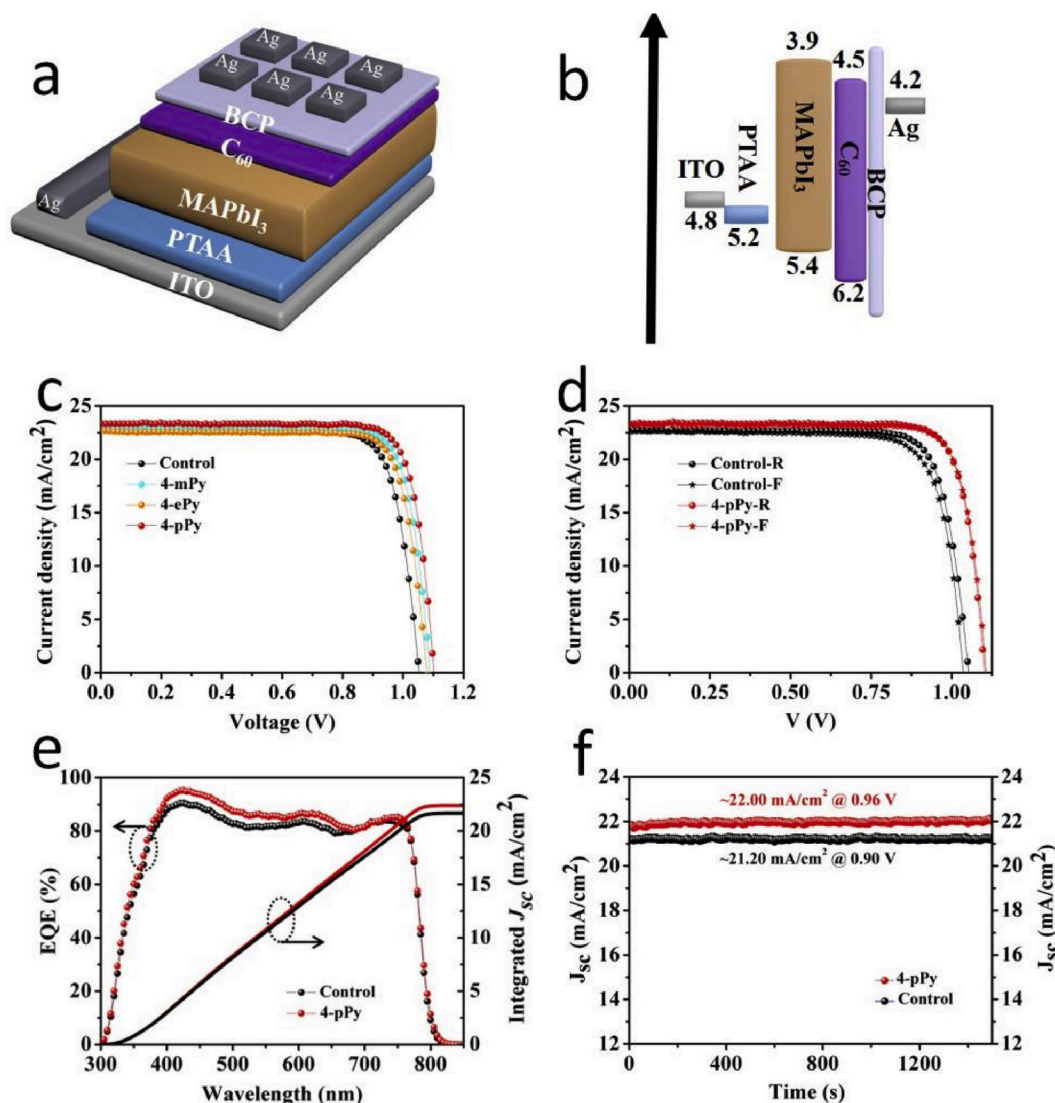
Fig. 3. a, b) Device structure and energy diagram of the perovskite solar cells. (c) Typical J-V curves of various PSCs. (d) J–V characteristics from forwarding scan (F, Jsc to Voc) and reverse scan (R, Voc to Jsc) determined under simulated AM 1.5G illumination for the controlled and 4-pPy modified devices. (e) IPCE and integrated current density of controlled and 4-pPy modified PSCs. (f) J-t curves of stabilized current density at MPP.

reduced concentration of iodide vacancies at the surfaces through Py-derivatives modification. To verify the theoretical prediction, thermal admittance spectroscopy (TAS) was conducted to characterize the trap density of states (t-DOS) in devices. This analysis is widely used in organic and perovskite solar cells for illustrating the defect state distribution information via the identification of junction capacitance. The experiment details and calculations of the t-DOS can be found in the supporting information [35,36]. As shown in Fig. 4d, a high density of defect states on the order of 1×10^{16} m^{-3} was estimated in the controlled devices. Interestingly, when the devices are made with Py-derivatives, the tDOS were substantially reduced by nearly one order of magnitude. The inhibition of trap states in Py-derivatives modified devices derived from the crystallization kinetics and surface passivation process, conducive to eliminating both the trap-induced non-radiative recombination and trap-induced volatilization of components.

In addition to the defects states, the internal charge transporting/ exchange behavior, as another important factor, should also be further elucidated. Transient photocurrent (TPC) measurement was conducted to measure the charge transit dynamic across the films after charge generation. As shown in Fig. 4i, the charge transient time of controlled, 4-mPy, 4-ePy and 4-pPy based PSCs was fitted as 4.56 μs, 3.88 μs, 4.67 μs

and 3.01 μs, respectively. Theoretically, a shorter photocurrent decay time was accompanied with the faster charge transfer in the device [30]. Here, 4-mPy and 4-pPy plays a positive role of charge transporting/exchange, and the latter is more effective. While 4-ePy failed to accelerate the charge. This can be rationalized by the analysis of the geometry and electronic properties of the surface ligands. Fig. 4e-h show the geometries of MAPbI$_3$ surfaces without and with considered Py-derivatives relaxed with DFT. Both the 4-mPy (Fig. 4f) and 4-pPy (Fig. 4h) exhibit the ordered orientation when anchoring on the surface of the perovskite, because of the planar structure of 4-pPy and the relatively small alkyl group in 4-mPy, respectively. In contrast, 4-ePy ligands exhibit the distorted orientation at the perovskite surface most possibly due to the steric effects between the alkyl (ethyl) groups in neighboring ligands. Fig. 4j-l show the electron-density distribution of the lowest unoccupied molecular orbitals (LUMOs) of the three Py-derivative molecules computed with DFT. We can observe that obvious electronic delocalization extended on the entire structure of 4-pPy, implying the excellent charge-transporting characteristic. On the contrary, the LUMO electron densify is nearly completely localized on the pyridine ring of 4-mPy and 4-pPy. Moreover, ordered ligands (4-mPy and 4-pPy) at the surfaces may establish direct charge-transporting
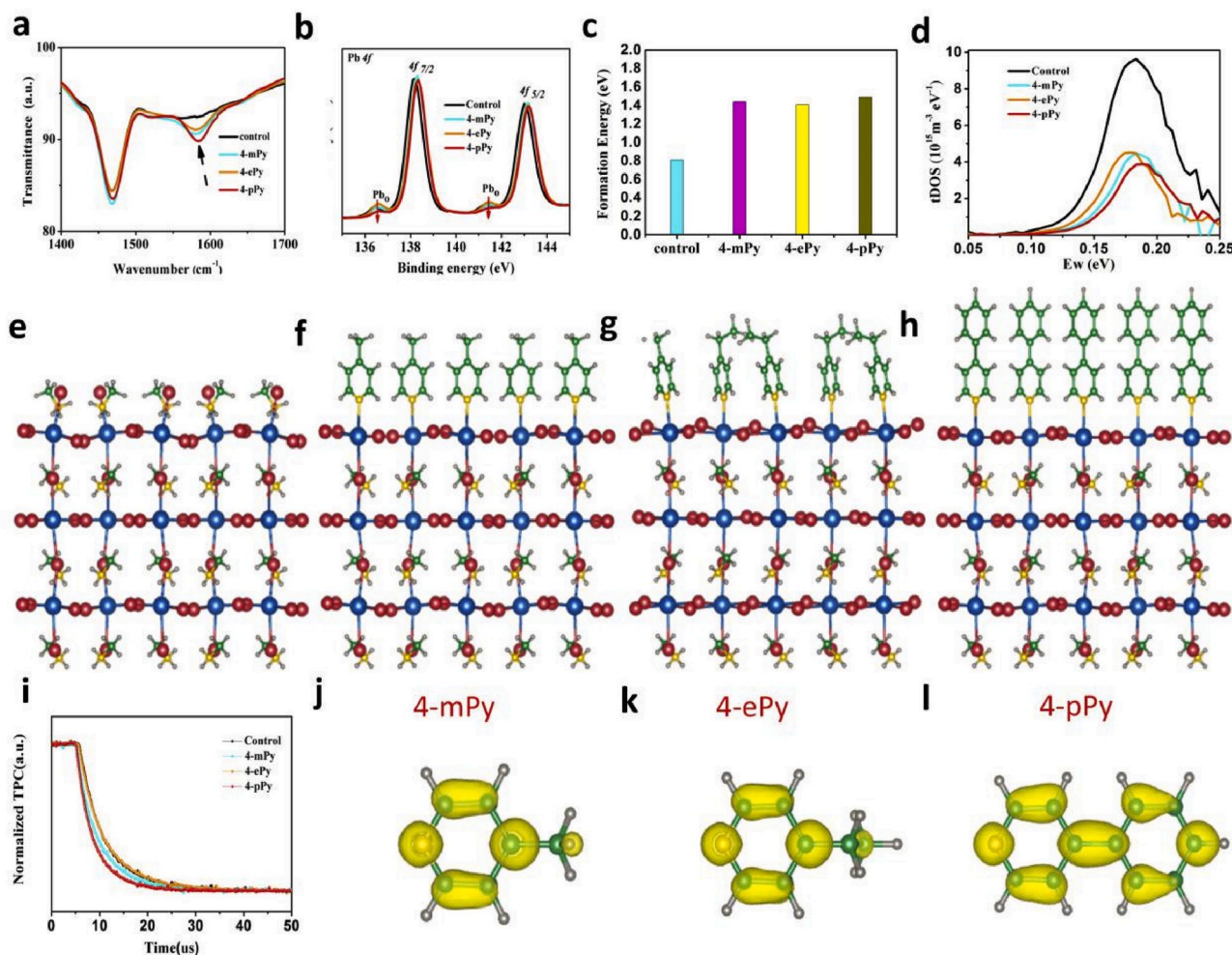
Fig. 4. (a) FTIR and (b) XPS analysis of controlled and Py-derivates modified perovskite films. (c) The formation energy of iodide vacancy by DFT calculation. (d) Trap density of states (tDOS) for the controlled device and the Py-derivates modified device. (e-h) DFT simulation of the steric arrangement of controlled and Py-derivates modified perovskite supercells. (i) TPC measurements of controlled and Py-derivates modified perovskite films. LUMO electron density distribution of (j) 4-mPy (k) 4-ePy and (l) 4-pPy molecules.

pathways between adjacent perovskite units or perovskite/transporting layer interface. With rigid and delocalized features, 4-pPy is entitled to own the advantageous charge-transporting properties in devices.

2.4. Stability investigation

The degradation of PSCs in the ambient environment is still of significant concern. We firstly compared the moisture-resistance of the controlled and modified MAPbI$_3$ films by exposing the samples in an atmosphere with ~60% RH. The static water contact angle was measured and the degradation process was traced by the color record and XRD measurements (Fig. S10). Undergoing 1500 h aging, it is noted that obvious color change was observed in the unmodified film, accompanied by the emerging PbI$_2$ peak. On the contrary, Py-derivatives modified films exhibited excellent moisture stability, suggested by nearly maintaining MAPbI$_3$ peaks. The outstanding water-repelling ability of the modified films can be attributed to the typical hydrophobic group (alkyl and phenyl) existing in the Py-derivatives. In order to evaluate the device stability, the devices with various perovskite films were stored in air with same humidity condition, and corresponding PCE evolution was recorded. As shown in Fig. 5a, the PCE of the controlled device fell to 20% of its original after 1000 h. Notably, all Py-derivatives modified devices still maintained ~90% of their original efficiency, indicating a profoundly reinforced environmental stability.

Other important factors influencing the stability of perovskite solar cells are thermal stress and illumination. Due to the vacancy defects and soft lattice characteristics of perovskite material, ion diffusion and vacancy formation would become severe under harsh conditions (high-temperature and continuous illumination). Previous studies have reported that the decomposition of perovskite preferentially occurs on GBs or surface, then gradually erodes the interior crystal structure. Based on the aforementioned discussion, Py-derivatives anchored on the GBs/ surface of the perovskite could effectively suppress the formation of the iodide vacancy, thus alleviating the ion diffusion/volatilization. With respect to the heat stress test, perovskite films and unencapsulated devices were kept under 85 °C continuous annealing. The degradation process of the films was traced by the color record and XRD measurements (Fig. S11). Undergoing 400 h aging, discernible color change was observed in the controlled and 4-ePy modified film, accompanied by the obviously PbI$_2$ peak. While, 4-mPy/4-pPy modified films maintained black phase. As shown in Fig. 5b, the thermal stability of Py-derivatives modified devices differed greatly compared with that of controlled devices. The 4-mPy/4-ePy/4-pPy based devices retained 85.4%/51.2%/ 89.2% of their initial PCE after annealing at 85 °C for 500 h, while the controlled device retains only 24% of its original PCE. Most importantly, the operational stability of unencapsulated devices under maximum power point (MPP) tracking with continuous one-sun illumination was investigated in the glove box (Nitrogen environment) (Fig. 5c). The PCE
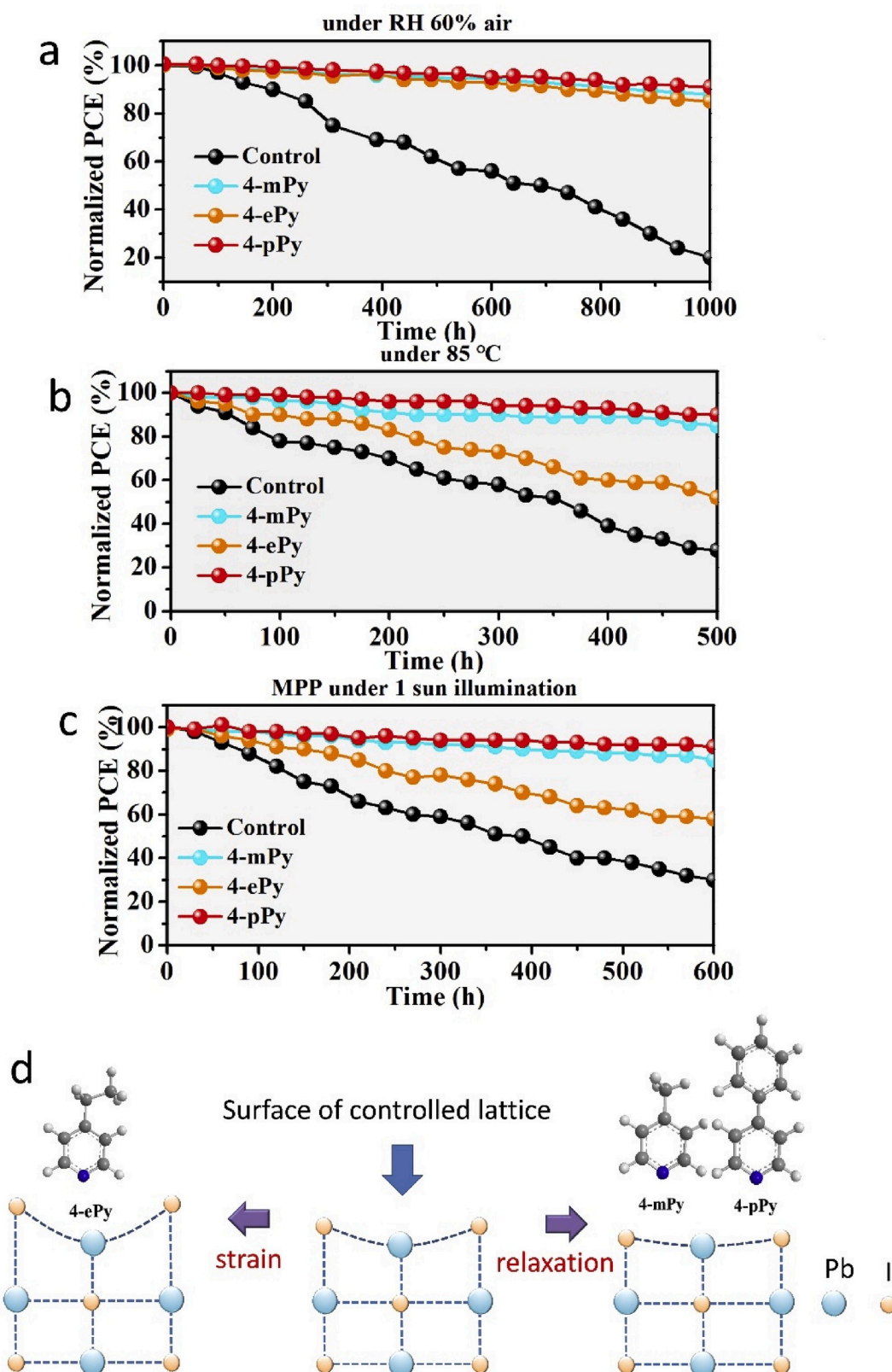
Fig. 5. The stabilities of the control and Py-derivates modified PSCs: a) Shelf stability of the devices with RH ~60% for 1000 h. b) thermal stability by putting the devices PSCs at 85 °C hot plate for 500 h. c) Operational stability of devices under continuous illumination for 600 h. d) Evolution of surface lattice strain regulated different Py-derivates.

degradation of controlled cells is rapid, showing a 28% life of the initial PCE after working for 600 h. While the PCE losses of 4-mPy/4-ePy/4-pPy based devices were 84.2%/57.4%/90.1% of its original PCE after 600 h.

Compared with the consistent moisture resistance of three Py-derivatives, the individual differential tolerance observed in the thermal/operating test is worth considering. Our discussion has shown that anchored Py-derivatives incorporated into the perovskite could effectively suppress the formation of the iodide vacancy, thus preventing the ion diffusion/volatilization. Based on the supercells mode by DFT calculation, it is noticed that although the formation energy of ion vacancy in Py-derivates modified films were pretty close, the coordination-induced distortion of the metal-iodide bond angle varied considerably. As estimated, the surface iodide-metal-iodide angle of controlled, 4-mPy, 4-ePy and 4-pPy modified supercells were 159°, 167°, 137° and 169°, respectively. It is suspected that Py-derivatives with rigid geometrical configuration (4-mPy, and 4-pPy) own the unidirectional orientation on the lattice surface, exerting the related uniform chemical interaction with the framework. Hence the shape change of the lattice is negligible relaxation. However, a flexible 4-ePy molecule just anchored on the lattice surface with the polydirectional distribution, and the asymmetrical chemical force may lead to the significant cage distortions and octahedra tilting (shown in Fig. 5d). Accordingly, the overloaded local strain of the lattice was deduced to lower the lattice stability under severe conditions, especially in high-temperature and operating stress.

3. Conclusion

In Conclusion, we have successfully achieved the dual regulation of crystal kinetics and lattice stabilization of perovskite films via pyridine-induced strategy. The chelation between pyridine molecule and the precursors of perovskite, which can effectively regulate the nucleation of the films and the crystal morphology of the perovskite films. In addition, the theoretical calculation of perovskite grain surface and pyridine derivatives molecules from DFT simulation of three-dimensional arrangement confirmed that the optimal configuration of different molecules, realizing the superiority with rigid 4-pPy instead of other two kinds of derivatives. Besides, ordered arrangement is available to significantly reduce the space of the lattice distortion. This facile approach could not only reduce the decomposition of perovskite films but also contribute to the excellent electrical properties. Employing 4-pPy rigid molecules in p-i-n planar heterojunction devices, the best 21.12% efficiency was yield, maintaining long-term stability under different harsh environments (90% of the initial PCE after 1000 h of 60% humidity testing, 89% of the initial PCE after 500 h of 85 °C testing, 90% of the initial PCE after 600 h of operating testing). We expect this work to provide a promising approach to strengthen perovskite photovoltaics and enlighten more excellent ligand molecules with similar properties being designed and applied for versatile electronic devices.

4. Experimental section

Materials and reagents: Methylamium Iodine (MAI, 99.99%), and poly [bis(4-phenyl) (2,4,6-trimethylphenyl)amine] (PTAA, Mn < 6000) were purchased from Xi'an Polymer Light Technology Corp (China). Lead diiodide (PbI$_2$, >99.99%) was purchased from TCI (Japan). 2,3,5,6-Tetrafluoro-7,7,8,8-tetracyanoquinodimethane (F4-TCNQ, 99.0%), bathocuproine (BCP, 99.0%), and buckminsterfullerene (C$_{60}$, 99%) were purchased from Nichem (Taiwan). The modulated materials, 4-methylpyridine (4-mPy), 4-ethylpyridine (4-ePy) and 4-phenylpyridine(4-pPy), were purchased from TCI (Japan) and used without purification. Besides, some reagents, including chlorobenene (CB, Extra Dry, 99.8%), N,N-dimethylformamide (DMF, anhydrous, 99.8%), and dimethyl sulfoxide (DMSO, anhydrous, 99.8+%) were purchased from commercial sources (Acros or Alfa Aesar) and used as received. Metal material silver was obtained from commercial sources (China New Metal Materials

Technology Co. Ltd.) with high purity (99.99%).

Perovskite precursor solution: A mixed solution of PbI$_2$ (1.3 M), and MAI (1.3 M) was dissolved in dimethylformamide (DMF) and dimethyl sulfoxide (DMSO) (7:3, v/v).

Doped-PTAA solution: We first obtained a solution of F4-TCNQ in CB (2 mg ml^{-1}), which was stirred at 70 °C for 15 min. F4-TCNQ solution was then added into PTAA solution (2 mg ml^{-1} in CB) with a weight ratio of 1%.

Hole-transport layer: The Indium tin oxide (ITO) patterned glass substrates with sheet resistance of about 15 Ω/square were cleaned with deionized water and organic solvents, and then expose to UV–ozone ambience for 15 min. The substrate's size is 2.5 × 2.5 cm^2. Then, the ITO substrates were transferred to a N$_2$-filled glovebox with H$_2$O and O$_2$ concentrations of <0.1 ppm. F4-TCNQ-doped PTAA solution was spin-coated onto the ITO substrates at 6000 rpm (with a ramping rate of 2000 rpm s-1), and the substrates were heated at 100 °C for 10 min in a N$_2$-filled glovebox.

Perovskite films deposition: The organic-inorganic lead halide perovskite solution, without or with Py-derivatives (5 mg ml^{-1}) modified, was spin-coated on the PTAA-coated ITO samples by a spinning process at 6000 rpm for 60 s with a ramping rate of 2000 rpm s^{-1}. During the spinning step, 800 μL of anhydrous CB was poured on the center of the spinning substrates 25 s prior to the end of the whole spinning process. Then, the films was quickly annealed by a two-step heating process at 60 °C for 1 min and 100 °C for 10 min.

Electron-transport layer and metal electrodes: C$_{60}$ (40 nm)/BCP(6 nm) were thermal evaporated at well-prepared-fresh perovskite coated substrats. Subsequently, the metal electrode Ag was thermally evaporated with the thinkness 120 nm. All of the thermal evaporation rate ranged from 0.1 to 2 Å s^{-1} depending on different materials used. And all of thermally evaporated steps were in a vacuum chamber with the base pressure of <4.5 × 10-4 Pa.

Materials and Solar cell characterization: A field emission scanning electron microscope (SEM) (Quanta 250, FEI, USA) was used to investigate the morphology and crystallinity. The crystalline structure on ITO substrate is performed by a X-ray diffractometer (Bruker D8 ADVANCE) with Cu Kα radiation. The absorption was obtained by UV–Vis spectrophotometer (HITACHI U-3010, Japan). The UPS/D-XPS characteristic were carried out by X-ray photoelectron spectroscopy (ESCALAB Xi+, Thermo Fisher Scientific). The photovoltaic performance was estimated under a AAA solar simulator (Zolix, China), AM 1.5G irradiation with an intensity of 100 mW cm^{-2}. The photocurrent-voltage (J-V) curve was measured by a Keithley (2602 Series Soureemeter), and the scan rates were performed by 0.2 V s^{-1} starting from −0.1 V to 1.2 V. The area of each device, calibrated by the shadow mask, was 4.92 mm^2.

Grazing-Incidence Wide Angle X-Ray Scattering: GIWAXS measurements were performed at the Shanghai Synchrotron Radiation Facility Laboratory on Beamline BL14B1 using X-ray with a wavelength of λ = ≈1.24 Å. 2D GIWAXS patterns were acquired by a MarCCD mounted vertically at a distance ≈194 mm from the sample with a grazing incidence angle of 0.4° and an exposure time of 50 s. The 2D GIWAXS patterns were analyzed using the FIT2D software and displayed in scattering vector q coordinates with q = 4πsinθ/λ, where θ is half of the diffraction angle and λ is the wavelength of incident X-ray.

Declaration of competing interest

The authors declared that they have no conflicts of interest to this work. We declare that we do not have any commercial or associative interest that represents a conflict of interest in connection with the work submitted.

CRediT authorship contribution statement

Jie Xu: Formal analysis, Writing - original draft. **Hua Dong:** Writing - original draft, Formal analysis, Supervision. **Yingguo Yang:** Formal

Appendix A. Supplementary data

Supplementary data to this article can be found online at https://doi.org/10.1016/j.nanoen.2020.104940.

References

[1] A. Kojima, K. Teshima, Y. Shirai, T. Miyasaka, J. Am. Chem. Soc. 131 (2009) 6050.
[2] H. chen, F. Ye, W. Tang, J. He, M. Yin, Y. Wang, F. Xie, E. Bi, X. Yang, M. Grätzel, L. Han, Nature 550 (2017) 92.
[3] L. Liu, S. Huang, Y. Lu, P. Liu, Y. Zhao, C. Shi, S. Zhang, J. Wu, H. Zhong, M. Sui, H. Zhou, H. Jin, Y. Li, Q. Chen, Adv. Mater. 30 (2018) 1800544.
[4] a) W. Sha, H. Zhang, Z. Wang, H. Zhu, X. Ren, F. Lin, A. Jen, W. Choy, Adv. Energy Mater. 8 (2018) 1701586;
b) J. Chen, H. Dong, L. Zhang, J. Li, F. Jia, B. Jiao, J. Xu, X. Hou, J. Liu, Zhaoxin Wu, J. Mater. Chem. (2020), https://doi.org/10.1039/c9ta11344d.
[5] Y. Rong, Y. Hu, A. Mei, H. Tan, M. Saidaminov, S. Seok, M. McGehee, E. Sargent, H. Han, Science 361 (2018) eaat8235.
[6] a) J. Song, J. Li, X. Li, L. Xu, Y. Dong, H. Zeng, Adv. Mater. 27 (2015) 7162;
b) J. Dai, J. Xi, Y. Zu, L. Li, J. Xu, Y. Shi, X. Liu, Q. Fan, J. Zhang, S. Wang, F. Yuan, H. Dong, B. Jiao, X. Hou, Z. Wu, Nano Energy 70 (2020) 104467;
c) Y. Zu, J. Xi, L. Li, J. Dai, S. Wang, F. Yun, B. Jiao, H. Dong, X. Hou, Z. Wu, ACS Appl. Mater. Interfaces 12 (2020) 2835.
[7] J. Song, L. Xu, J. Li, J. Xue, Y. Dong, X. Li, H. Zeng, Adv. Mater. 28 (2016) 4861.
[8] Z. Xiao, Y. Yan, Adv. Energy Mater. 7 (2017) 1701136.
[9] S. Stranks, G. Eperon, G. Grancini, C. Menelaou, M. Alcocer, T. Leijtens, L. Herz, A. Petrozza, H. Snaith, Science 342 (2013) 341.
[10] C. Boyd, R. Cheacharoen, T. Leijtens, M. McGehee, Chem. Rev. 119 (2019) 5.
[11] NREL. Best Research-Cell Efficiencies. https://www.nrel.gov/pv/assets/pdfs/best-research-cell-efficiencies.20190802.pdf.
[12] J. Correa-Baena, M. Saliba, T. Buonassisi, M. Grätzel, A. Abate, W. Tress, A. Hagfeldt, Science 358 (2017) 739.
[13] R. Wang, M. Mujahid, Y. Duan, Z. Wang, J. Xue, Y. Yang, Adv. Funct. Mater. 29 (2019) 1808843.
[14] L. Wang, H. Zhou, J. Hu, B. Huang, M. Sun, B. Dong, G. Zheng, Y. Huang, Y. Chen, L. Li, Z. Xu, N. Li, Z. Liu, Q. Chen, L. Sun, C. Yan, Science 363 (2019) 265.
[15] N. Li, S. Tao, Y. Chen, X. Niu, C. Onwudinanti, C. Hu, Z. Qiu, Z. Xu, G. Zheng, L. Wang, Y. Zhang, L. Li, H. Liu, Y. Lun, J. Hong, X. Wang, Y. Liu, H. Xie, Y. Gao, Y. Bai, S. Yang, G. Brocks, Q. Chen, H. Zhou, Nat. Energy 4 (2019) 408.
[16] N. Noel, A. Abate, S. Stranks, E. Parrott, V. Burlakov, A. Goriely, H. Snaith, ACS Nano 8 (2014) 9815–9821.
[17] F. Wang, W. Geng, Y. Zhou, H. Fang, C. Tong, M. Loi, L. Liu, N. Zhao, Adv. Mater. 28 (2016) 9986–9992.
[18] J. Lee, H. Kim, N. Park, Acc. Chem. Res. 49 (2016) 311.
[19] J. Lee, S. Bae, Y. Hsieh, N. Marco, M. Wang, P. Sun, Y. Yang, Chem 3 (2017) 290.
[20] J. Lee, Z. Dai, C. Lee, H. Lee, T. Han, N. Marco, O. Lin, C. Choi, B. Dunn, J. Koh, Dino D. Carlo, J. Ko, H. Maynard, Y. Yang, J. Am. Chem. Soc. 140 (2018) 6317.
[21] Q. Tai, P. You, H. Sang, Z. Liu, C. Hu, H. Chan, F. Yan, Nat. Commun. 7 (2016) 11105.
[22] W. Ke, C. Xiao, C. Wang, B. Saparov, H. Duan, D. Zhao, Z. Xiao, P. Schulz, S. Harvey, W. Liao, W. Meng, Y. Yu, A. Cimaroli, C. Jiang, K. Zhu, M. Al-Jassim, G. Fang, D. Mitzi, Y. Yan, Adv. Mater. 28 (2016) 5214.
[23] H. Dong, Z. Wu, J. Xi, X. Xu, L. Zuo, T. Lei, X. Zhao, L. Zhang, X. Hou, A. Jen, Adv. Funct. Mater. 28 (2018) 1704836.
[24] J. Chen, J. Seo, N. Park, Adv. Energy Mater. 8 (2018) 1702714.
[25] Y. Bai, S. Xiao, C. Hu, T. Zhang, X. Meng, H. Lin, Y. Yang, S. Yang, Adv. Energy Mater. 7 (2017) 1701038.
[26] K. Yao, X. Wang, F. Li L. Zhou, Chem. Commun. 51 (2015) 15430.
[27] L. Li, Z. Sun, P. Wang, W. Hu, S. Wang, C. Ji, M. Hong, J. Luo, Angew. Chem. Int. Ed. 56 (2017) 12150.
[28] C. Ma, C. Leng, Y. Ji, X. Wei, K. Sun, L. Tang, J. Yang, W. Luo, C. Li, Y. Deng, S. Feng, J. Shen, S. Lu, C. Du, H. Shi, Nanoscale 8 (2016) 18309.
[29] D. Yu, B. Cai, F. Cao, X. Li, X. Liu, Y. Zhu, J. Ji, Y. Gu, H. Zeng, Adv. Mater. Interfaces 4 (2017) 1700441.
[30] Z. Wang, M. Li, Y. Yang, Y. Hu, H. Ma, X. Gao, L. Liao, Adv. Mater. 28 (2016) 6695–6703.
[31] Published by Bio-Rad Laboratories, Inc., Informatics Division. © 1978-2004 Bio-Rad Laboratories, Inc. All Rights Reserved.
[32] D. Bi, X. Li, J. Milić, D. Kubicki, N. Pellet, J. Luo, T. LaGrange, P. Mettraux, L. Emsley, S. Zakeeruddin, M. Grätzel, Nat. Commun. 9 (2018) 4482.
[33] D. Bi, C. Yi, J. Luo, J. Décoppet1, F. Zhang, S. Zakeeruddin, X. Li, A. Hagfeldt, M. Grätzel, Nat. Energy 1 (2016) 16142.
[34] W. Deng, X. Liang, P. Kubiak, P. Cameron, Adv. Energy Mater. 8 (2018) 1701544.
[35] Y. Shao, Y. Yuan, J. Huang, Nat. Energy 1 (2016) 15001.
[36] N. Li, S. Ta, Y. Chen, X. Niu, C. Onwudinanti, C. Hu, Z. Qiu, Z. Xu, G. Zheng, L. Wang, Y. Zhang, L. Li, H. Liu, Y. Lun, J. Hong, X. Wang, Y. Liu, H. Xie, Y. Gao, Y. Bai, S. Yang, G. Brocks, Q. Chen, H. Zhou, Nat. Energy 4 (2019) 408.